

This is an Open Access document downloaded from ORCA, Cardiff University's institutional repository: <https://orca.cardiff.ac.uk/id/eprint/112315/>

This is the author's version of a work that was submitted to / accepted for publication.

Citation for final published version:

Kim, Hyunseok, Lee, Wook-Jae , Farrell, Alan C., Balgarkashi, Akshay and Huffaker, Diana L. 2017. Telecom-wavelength bottom-up nanobeam lasers on silicon-on-insulator. *Nano Letters* 17 (9) , pp. 5244-5250. 10.1021/acs.nanolett.7b01360

Publishers page: <http://doi.org/10.1021/acs.nanolett.7b01360>

Please note:

Changes made as a result of publishing processes such as copy-editing, formatting and page numbers may not be reflected in this version. For the definitive version of this publication, please refer to the published source. You are advised to consult the publisher's version if you wish to cite this paper.

This version is being made available in accordance with publisher policies. See <http://orca.cf.ac.uk/policies.html> for usage policies. Copyright and moral rights for publications made available in ORCA are retained by the copyright holders.



# Telecom-wavelength Bottom-up Nanobeam Lasers on Silicon-on-Insulator

*Hyunseok Kim<sup>1,\*</sup>, Wook-Jae Lee<sup>2</sup>, Alan C. Farrell<sup>1</sup>, Akshay Balgarkashi<sup>3</sup> & Diana L. Huffaker<sup>1,3,4</sup>*

<sup>1</sup>Department of Electrical Engineering, University of California Los Angeles, Los Angeles, California 90095, United States

<sup>2</sup>School of Engineering, Cardiff University, Cardiff CF24 3AA, United Kingdom

<sup>3</sup>School of Physics and Astronomy, Cardiff University, Cardiff CF24 3AA, United Kingdom

<sup>4</sup>California Nano-Systems Institute, University of California Los Angeles, Los Angeles, California 90095, United States

Keywords

Nanowire laser, nanobeam, telecom wavelength, room temperature, monolithic integration

## **Abstract**

Semiconductor nanowire lasers are considered promising ultra-compact and energy-efficient light sources in the field of nanophotonics. Although the integration of nanowire lasers onto silicon photonic platforms is an innovative path towards chip-scale optical communications and photonic integrated circuits, operating nanowire lasers at telecom-wavelengths remains challenging. Here, we report on InGaAs nanowire array lasers on a silicon-on-insulator platform operating up to 1,440 nm at room temperature. Bottom-up photonic crystal nanobeam cavities are formed by growing nanowires as ordered arrays using selective-area epitaxy, and single-mode lasing by optical pumping is demonstrated. We also show that arrays of nanobeam lasers with individually tunable wavelengths can be integrated on a single chip by simple adjustment of the lithographically defined growth pattern. These results exemplify a practical approach towards nanowire lasers for silicon photonics.

Semiconductor nanowires are a promising platform for ultracompact lasers, which have high potential in the field of optical communications, bio- and chemical sensing, and quantum computing. As nanowires provide both gain from their bulk volume and optical feedback from their end facets (Fabry–Perot cavity), a single nanowire can operate as a sub-wavelength scale nanolaser without the need for external cavities. In particular, the high crystal quality of nanowires<sup>1</sup> and the ability to incorporate three-dimensional heterostructures<sup>2</sup> enable the nanowires to exhibit superior optical properties, while atomic-scale sidewall smoothness and large refractive indices ensure nanowire Fabry–Perot cavities to exhibit strong mode confinement and to achieve sufficient cavity quality ( $Q$ ) factor<sup>3</sup>. By exploiting these notable features, nanowire lasers operating in ultraviolet, visible, and near-infrared wavelengths have been reported using both III-V and II-VI material systems<sup>3-6</sup>.

Because nanowires can be grown on lattice-mismatched substrates owing to nanoscale interface areas, directly integrating nanowire lasers on silicon has also gained attention to utilize these nanolasers for silicon photonics and ultracompact inter- and intrachip optical communications. Contrary to typical nanowire lasers which attain strong optical feedback by horizontally laying nanowires onto low-index substrates, the achievement of lasing in vertical free-standing nanowires on silicon is challenging because the small index contrast between the nanowires and the substrate results in low reflectivity at the bottom interface. Several approaches have been proposed to overcome this limitation and to observe lasing from nanowires on silicon, such as employing a helical cavity mode<sup>7</sup>, enhancing the reflectivity by selective etching<sup>8</sup>, inserting an interlayer<sup>9</sup>, and forming random cavities comprised of tapered nanowires<sup>10</sup>.

However, practical integration of nanowire lasers on silicon photonic integrated circuits (PICs) continues to be a significant challenge. To the best of our knowledge, there are no reports of monolithic nanowire lasers on silicon operating in the telecom-wavelength range.

This may be attributed to difficulties in growing high-quality nanowires with proper bandgaps on silicon<sup>11</sup>, as well as non-radiative Auger recombination which increases as the bandgap is decreased<sup>5,12</sup>. Furthermore, the confinement factor and end-facet reflectivity decrease at longer wavelengths in sub-wavelength scale nanowire cavities, implying that the nanowire diameter and length must increase to support longer wavelength lasing<sup>13</sup>. Operation wavelengths of vertical free-standing nanowire lasers on silicon have thus been limited to shorter wavelengths ( $<1,230$  nm)<sup>7-9</sup>, and telecom-wavelength lasing from nanowires has been achieved only at cryogenic temperatures by heterogeneous integration methods, such as transferring nanowires onto external cavities<sup>14</sup> and dispersing microwires (wire diameter  $\sim 1$   $\mu\text{m}$ , wire length  $\sim 30$   $\mu\text{m}$ ) on low-index substrates<sup>15</sup>.

Controlling or selecting the lasing mode of nanowire lasers is another challenge, while this is a crucial requirement for practical applications. The emission from single nanowire lasers is typically multimode, owing to a dense mode spacing in longitudinal Fabry–Perot modes which is inversely proportional to the length of nanowires<sup>6</sup>. Slight changes in temperature, alloy composition, or pump power can lead to the excitement of a different cavity mode<sup>13</sup>. Although recent advances have shown that single-mode lasing can be achieved from free-standing nanowires by forming nanowire arrays<sup>10,16</sup> or growing nanowires on distributed Bragg reflectors<sup>17</sup>, the lasing wavelengths are still limited to short wavelengths ( $< 1,130$  nm).

Here, we demonstrate telecom-wavelength nanowire lasers on a silicon-on-insulator (SOI) platform operating in a single mode at room temperature. Instead of employing single nanowire laser cavities, we form one-dimensional (1D) photonic crystal nanobeam cavities by growing nanowires as 1D arrays on patterned SOI substrates. This approach significantly increases the cavity  $Q$  factor and enables the control of the lasing wavelength by lithography, resulting in a single-mode operation. Lasing wavelengths range from 1,100 nm to 1,440 nm, which is achieved by optimizing the growth condition of InGaAs nanowires and InGaP shells

using catalyst-free metal-organic chemical vapor deposition (MOCVD). Telecom-wavelength lasing from monolithic laser arrays on a single chip and high accuracy in controlling the lasing wavelengths indicate that our approach could be a key enabling technology for next-generation chip-scale optical links.

The schematic illustration of the nanowire array laser on an SOI(111) substrate is depicted in Figure 1a. A total of 31 vertical nanowires constitute a 1D photonic crystal cavity, which is also known as a nanobeam cavity. InGaAs nanowires are employed as a gain medium, which are passivated by thin InGaP shells to reduce non-radiative surface recombination. 3D field confinement is achieved in the proposed nanobeam cavities by a photonic bandgap in one dimension along the nanowires and total internal reflection in the other two dimensions through refractive index contrast (detailed cavity design in Supporting Information Section I). The nanowires at both sides composing the reflector section (20 nanowires) are evenly spaced to form a photonic bandgap along the  $x$ -axis. On the other hand, the distances of nanowires in the center (11 nanowires) are linearly tapered, which locally modulates the mode gap edge and creates a confined mode in the tapered section<sup>18,19</sup>. A 220 nm-thick SOI layer is employed, which is a standard thickness in silicon photonic foundries<sup>20</sup>, to verify the compatibility of the proposed nanobeam lasers with silicon photonic platforms. Silicon trenches with a depth of 180 nm are formed around each nanowire to attain a high cavity  $Q$  factor by reducing the leakage of the optical field through the silicon layer<sup>16</sup>. As a TE-mode photonic bandgap typically does not exist or is smaller than a TM-mode bandgap in rod-type photonic crystals, we utilize a TM-mode (electric field along the  $z$ -axis) as the lasing mode<sup>21</sup>. The fundamental TM-mode profiles of nanobeam cavities with various dimensions are calculated by 3D finite-difference time-domain (FDTD) simulations. As an example, Figures 1b and 1c show electric field profiles ( $E_z$ ) of the fundamental TM-mode when the nanobeam cavity dimensions are set to  $p = 350$  nm,  $d = 180$  nm, and  $h = 700$  nm. The field is tightly confined in the nanowires in

the tapered section, corresponding to a confinement factor of  $\Gamma = 0.548$  and  $Q = 134,000$  at a resonant wavelength of 1,310 nm, where such a high confinement factor and cavity  $Q$  factor can lead to low-threshold lasing and fast modulation speeds. It should also be noted that the resonance wavelength of nanobeam cavities can be controlled by changing the lattice constant and the fill factor of photonic crystals, which correspond to the period ( $p$ ) and diameter ( $d$ ) in our design.

A catalyst-free selective-area epitaxy (SAE) technique is employed to grow InGaAs nanowires by MOCVD. The SAE approach enables precise positioning of vertical nanowires on pre-patterned SOI substrates without contaminating silicon with metallic catalysts, because nanowire growth is initiated from exposed nanoholes in dielectric masks<sup>22,23</sup>. In the SAE method, however, it is challenging to grow InGaAs nanowires on silicon with high growth yield, uniformity, and intermediate indium composition to cover the telecom-wavelength range<sup>11</sup>. Also, incorporation of adatoms on nanowire side facets leads to a non-negligible increase of the nanowire diameter<sup>24</sup>. The nanowire epitaxy condition is, therefore, optimized to realize perfectly grown nanowire arrays with both the material composition and nanowire dimension matched to the design. Several samples with various cavity dimensions and indium compositions ( $x$ ) in  $\text{In}_x\text{Ga}_{1-x}\text{As}$  nanowires are grown to demonstrate lasing over a wide wavelength range including telecom-wavelengths. First, a thin GaAs seed layer is grown in nanoholes at 680 °C, because GaAs seeding increases the vertical growth yield of nanowires to almost 100 %, which is not achieved by directly growing InGaAs nanowires on SOI without seed layers (Supporting Information Figure S4). Next, the temperature is ramped down and InGaAs nanowires are grown on top of the GaAs seeding layer. We have found that the indium and gallium flux, and the temperature are critical factors affecting the growth rates of InGaAs nanowires along axial and radial directions. The axial and radial growth rates decrease and increase, respectively, when the indium flux ( $\Phi_{\text{In}/(\text{In}+\text{Ga})}$ ) is increased, while they increase and

decrease when the temperature is decreased (Supporting Information Figure S5). Therefore, InGaAs nanowires with higher  $x$  are grown at lower growth temperatures to suppress the growth along the radial direction and satisfy the nanobeam cavity design. Lastly, InGaAs nanowires are capped by InGaP shells to reduce non-radiative surface recombination. The material composition of the InGaP shell is varied according to the composition of InGaAs nanowires in order to closely match the lattice constant and ensure high core/shell interface quality. Detailed sample preparation and growth procedures are described in Methods section.

Nanowire arrays integrated on an SOI platform are depicted in the scanning electron microscope (SEM) images in Figure 2. Vertically grown InGaAs/InGaP core/shell nanowires exhibit smooth sidewalls and high uniformity in both the height and diameter between nanowires. Nanowire side facets are aligned perpendicular to the photonic lattice to achieve structural symmetry and high  $Q$  factor, as shown in Figure 2c, which is realized by patterning nanohole arrays along the  $\langle 110 \rangle$  direction of the silicon layer.

The photoluminescence (PL) spectra of nanowires are measured at room temperature using a spectrometer (SP-2500i, Princeton Instruments) and an InGaAs focal plane array detector (2D-OMA, Princeton Instruments) to characterize optical properties of the nanowires and to demonstrate lasing characteristics. A pulsed laser with 660 nm wavelength, 30 ps pulse width, and 78 MHz repetition rate is focused vertically onto the nanowires using a  $50\times$  objective lens ( $NA = 0.42$ ) for excitation with a pump spot size of  $2\ \mu\text{m}$ , and the emission from the nanowires is collected by the same lens and resolved by the spectrometer (Supporting Information Figure S6). Samples are mounted on a piezoelectric stage to precisely control the sample position. Figure 3a shows PL spectra of nanowire arrays ( $50 \times 50$  square lattice arrays with a pitch of  $1\ \mu\text{m}$ ) grown on planar areas without silicon trenches. Broad spontaneous emission is observed because nanowire arrays on 220 nm-thick SOI layers do not form cavities. The emission peak positions are observed around 1,150 nm, 1,240 nm, 1,370 nm, and 1,470

nm for the samples grown under different conditions, which correspond to approximate  $x$  of 0.26, 0.33, 0.42, and 0.48, respectively. The full width at half-maximum (FWHM) of the spontaneous emission is broad ( $> 120$  meV) at room temperature regardless of  $x$ , which is attributed to compositional fluctuations and polytypism in nanowires<sup>22,23</sup> (Supporting Information Figure S7 and S8).

Nanowire array cavities with different photonic lattice periods and fill factors are also grown on each sample by lithographically controlling the period ( $p$ ) and diameter ( $d$ ). Figure 3b shows lasing spectra from one of the nanobeam cavities on each sample with different  $x$ , which are measured by aligning the pump beam to the center of the cavities. As the pump spot size is  $2\ \mu\text{m}$ , the pumping area covers only the tapered section of the cavity. Lasing at longer wavelength is observed from the nanowire arrays with higher  $x$  and larger  $p$  and  $d$ , where the lasing peak positions at 1,120 nm, 1,230 nm, 1,320 nm, and 1,440 nm overlap well with the spontaneous emission spectra in Figure 3a. The light-in–light-out (L-L) plot, which represents an integrated cavity peak intensity as a function of the input pump power, is shown in Figure 3c for these four nanowire array lasers. Threshold pump powers of these lasers are estimated to be around  $80\text{--}110\ \mu\text{J}/\text{cm}^2$ , which are deduced from the position of the kinks in the linear fitting. It is interesting to note that the slope efficiency (differential quantum efficiency) shows a tendency to decrease if the laser operates at a longer wavelength, except the laser emitting at 1,230nm which shows a higher slope efficiency than the laser emitting at 1,120 nm. This tendency can be understood considering an exponential increase of Auger recombination coefficient for InGaAs with larger  $x$ <sup>25</sup>, which drastically increases non-radiative recombination at high-level carrier injection and decreases the internal quantum efficiency which is proportional to the slope efficiency<sup>26</sup>. We speculate that the reversed tendency between 1,120 nm and 1,230 nm lasers is stemming from the radiative efficiency of  $\text{In}_{0.33}\text{Ga}_{0.67}\text{As}$  nanowires being higher than  $\text{In}_{0.26}\text{Ga}_{0.74}\text{As}$  nanowires (Supporting Information Figure S10), which could

be due to the material quality or core/shell interface quality. It should be highlighted that this is the first demonstration of monolithic nanowire lasers on a silicon platform operating at telecom-wavelengths. Room-temperature lasing in these vertical free-standing nanowire arrays reveals the validity of our approach in attaining a high cavity  $Q$  and confinement factor by forming bottom-up nanowire photonic crystals and achieving sufficient gain from InGaP-passivated InGaAs nanowires.

Lasing characteristics of the laser operating at 1,320 nm, which exhibits a lasing threshold of  $95 \mu\text{J}/\text{cm}^2$  (Figure 3c), are further analyzed to demonstrate typical behaviors of optically pumped nanowire array lasers operating in the telecom-wavelength regime. Log-scale PL spectra in Figure 4a show relative emission intensities from the nanobeam laser when the input pump power is varied. A small cavity peak is observed above a broad spontaneous emission spectrum when the pump power is low. As the pump power is increased, the spontaneous peak blue-shifts due to a band-filling effect and the cavity peak also slightly blue-shifts due to a carrier-induced change of the refractive index<sup>27</sup>. The cavity peak intensity rapidly grows as the pump power is increased, while spontaneous emission is clamped above the lasing threshold, resulting in a side-mode suppression ratio (SMSR) of 13 dB at 2.55 times the threshold power. This is in contrast to the spontaneous emission from nanowire arrays on a planar area of a 220 nm-thick SOI substrate, which is not clamped by increasing the pump power (Figure 4b). The cavity peak linewidth shows a sudden decrease around the lasing threshold, as depicted in Figure 4c, which is another indication of lasing action. The linewidth above the threshold is relatively high at around 2 meV, which is attributed to a pumping by ultrashort pulses that leads to a significant linewidth broadening by refractive index fluctuation<sup>6,28</sup>. A double-logarithmic plot of the L-L curve in Figure 4c shows an S-shape response, which indicates the transition to lasing from amplified spontaneous emission (ASE). A standard rate equation analysis is employed to extract a  $Q$  factor and a spontaneous emission

factor  $\beta$  (Supporting Information Section II), which represents the portion of emitted photons coupled into a lasing mode. The  $Q$  factor of 495 is derived from the fitting which is significantly smaller than the  $Q$  factor calculated from the FDTD simulations, and this is attributed to fabrication imperfections and pumping conditions (Supporting Information Section I and II).  $\beta$  of 0.16 is extracted from the rate equation fitting, where such a large  $\beta$  can only be accomplished from cavities with ultra-small mode volume and/or high cavity  $Q$  factor<sup>26</sup>. This result suggests that the proposed bottom-up nanobeam lasers have high potential for energy-efficient light sources with extremely low threshold. The double-logarithmic L-L plots of lasers with different  $x$  and lasing wavelengths (inset in Figure 3c) show that slopes of integrated cavity peak intensities of these lasers are all different below and around the threshold. This implies that  $\beta$  of these lasers will all vary, while further study is necessary to understand the main factors governing these differences.

One of the biggest advantages of our approach is that the lasing wavelength is determined from nanobeam cavity dimensions, which can be controlled by lithography. Laser arrays with various operation wavelengths can, therefore, be integrated on a single chip by lithographically varying the pitch and diameter of nanowires, which suggests the possibility for an ultracompact light source in wavelength-division multiplexing (WDM) systems. Figure 5a shows lasing spectra of seven  $\text{In}_{0.33}\text{Ga}_{0.67}\text{As}$  nanowire array lasers, which are grown on two SOI pieces under identical epitaxy conditions. The measured lasing wavelengths range from 1,187 nm to 1,256 nm, which reveals wide tunability of the operation wavelengths of laser arrays on a chip. The validity and accuracy of tuning the lasing wavelength by lithography are also demonstrated by comparing the measured wavelengths with FDTD simulations, as shown in Figure 5b. The lasing wavelengths of entire nanowire array lasers with different indium compositions ( $x = 0.26, 0.33, 0.42, \text{ and } 0.48$ ) (filled stars) are plotted together with nanowire array cavities which have not reached lasing due to the mismatch between the indium

composition and the cavity mode wavelength (open stars) (Supporting Information Figure S11). As there is a slight non-uniformity between diameters of the nanowires constituting nanowire array cavities (typical standard deviation  $\sim 5$  nm), an average value of nanowire diameters in the tapered section is used as the measured diameter in Figure 5b. The measured peak wavelengths show a clear dependence on the period and diameter, and exhibit a good agreement with FDTD results (lines) within  $\pm 20$  nm error, substantiating the feasibility of wavelength control without the need of external cavities. We speculate several reasons for the error, such as nanowire diameter fluctuation, fabrication errors in silicon trench patterns, possible difference between the actual refractive index of nanowires and the index employed for FDTD simulations ( $n = 3.62$ ), and a non-negligible effect of the nanowire height on a cavity mode wavelength as the height of nanowires does not match exactly with simulations ( $h = 700$  nm) (Supporting Information Figure S12). The demonstration of nanobeam laser arrays on an SOI substrate with controllable lasing wavelengths suggests that the proposed nanolasers have high potential for chip-scale optical interconnects.

In conclusion, we have demonstrated monolithic nanowire array lasers on an SOI platform operating in the wavelength range of 1,100 nm – 1,440 nm. Room-temperature lasing from these lasers is achieved by optical pumping, which reveals that nanobeam cavities composed of InGaAs/InGaP core/shell nanowires exhibit high crystal quality and superior cavity properties. Lithographic control of nanobeam cavity dimensions has facilitated monolithic integration of laser arrays on a single chip with various wavelengths, suggesting a path towards an ultracompact light source in WDM systems. Although continuous-wave lasing at room temperature is not demonstrated due to thermal roll-over of fabricated devices, we speculate that improving the uniformity of nanowire dimensions, and the quality of passivation shells by optimizing the fabrication and growth conditions will enable continuous-wave lasing operation by reduced threshold gain and enhanced radiative efficiency. Electrical injection of

nanowire array lasers will be the next step for practical application to chip-scale data communications, which could be accomplished by growing doped nanowire arrays on doped SOI substrates followed by metallization. We believe that the proposed nanolasers can also be applied to low-cost and multi-spectral sensing platforms, quantum computing, and all-optical circuits.

## Methods

**Fabrication.** A lightly p-doped (10  $\Omega$ .cm) SOI(111) wafer is used as a growth platform. First, trench patterns are defined by standard electron-beam lithography. Then, a mixture of SF<sub>6</sub>, CF<sub>4</sub>, and CHF<sub>3</sub> plasma is used to etch 180 nm-deep trenches on 220 nm-thick SOI layers using ZEP520A resist as an etch-mask. A 20 nm-thick silicon nitride (Si<sub>3</sub>N<sub>4</sub>) mask is then deposited using low-pressure chemical vapor deposition on the patterned substrate, followed by electron-beam lithography and dry etching to pattern nanoholes and expose silicon for selective-area growth.

**Nanowire growth.** The MOCVD growth is carried out in a low-pressure (60 Torr) vertical reactor, using hydrogen as a carrier gas and triethylgallium (TEGa), trimethylindium (TMIn), tertiarybutylarsine (TBA), and tertiarybutylphosphine (TBP) as precursors. The sample is first baked at 850 °C for 10 min flowing hydrogen to thermally etch native oxide. Next, GaAs seeds are grown in nanoholes at 680 °C for 3 min under the partial pressure of TEGa =  $2.25 \times 10^{-5}$  atm and TBA =  $2.02 \times 10^{-3}$  atm. InGaAs nanowires are then grown for 13 min under different growth temperatures and partial pressures to tune the indium composition. The partial pressures and temperatures used are, TEGa =  $2.06 \times 10^{-5}$  atm and TMIn =  $8.70 \times 10^{-6}$  atm at 680 °C for In<sub>0.26</sub>Ga<sub>0.74</sub>As, TEGa =  $1.76 \times 10^{-5}$  atm and TMIn =  $1.18 \times 10^{-5}$  atm at 665 °C for In<sub>0.33</sub>Ga<sub>0.67</sub>As, TEGa =  $1.61 \times 10^{-5}$  atm and TMIn =  $1.32 \times 10^{-5}$  atm at 655 °C for In<sub>0.42</sub>Ga<sub>0.58</sub>As, and TEGa =  $1.61 \times 10^{-5}$  atm and TMIn =  $1.32 \times 10^{-5}$  atm at 635 °C for In<sub>0.48</sub>Ga<sub>0.52</sub>As, where TBA is fixed to  $2.02 \times 10^{-3}$  atm in all growths. Next, In(Ga)P shells are grown at 600 °C for 35 s under different partial pressures to closely lattice-match the shell with the InGaAs core. The partial pressures used are, TEGa =  $2.25 \times 10^{-6}$  atm, TMIn =  $6.63 \times 10^{-6}$  atm and TBP =  $4.26 \times 10^{-4}$  atm on In<sub>0.26</sub>Ga<sub>0.74</sub>As, TEGa =  $1.76 \times 10^{-6}$  atm, TMIn =  $1.18 \times 10^{-5}$  atm and TBP =  $4.39 \times 10^{-4}$  atm on In<sub>0.33</sub>Ga<sub>0.67</sub>As, and TMIn =  $1.03 \times 10^{-5}$  atm and TBP =

$1.55 \times 10^{-3}$  atm on  $\text{In}_{0.42}\text{Ga}_{0.58}\text{As}$  and  $\text{In}_{0.48}\text{Ga}_{0.52}\text{As}$ . After the growth, samples are cooled down to 300 °C by flowing TBP to prevent nanowire desorption.

### **Associated content**

Supporting Information. The Supporting Information is available free of charge on the ACS Publications website.

Nanobeam cavity design. Rate equation analysis. Nanowire growth condition. Measurement setup. Optical properties of nanowires. Nanobeam cavity emission characteristics. FDTD simulations of cavity mode wavelengths.

### **Author information**

Corresponding author

\*E-mail: [hyunseokkim@ucla.edu](mailto:hyunseokkim@ucla.edu)

### **Acknowledgements**

The authors gratefully acknowledge the generous financial support of this research by AFOSR (through FA9550-15-1-0324) and Sêr Cymru National Research Network in Advanced Engineering and Materials.

### **Competing financial interests**

The authors declare no competing financial interests.

## References

- 1 Caroff, P.; Dick, K. A.; Johansson, J.; Messing, M. E.; Deppert, K.; Samuelson, L. *Nat. Nanotechnol.* **2009**, *4*, 50-55.
- 2 Tomioka, K.; Yoshimura, M.; Fukui, T. *Nature* **2012**, *488*, 189-192.
- 3 Huang, M. H.; Mao, S.; Feick, H.; Yan, H.; Wu, Y.; Kind, H.; Weber, E.; Russo, R.; Yang, P. *Science* **2001**, *292*, 1897-1899.
- 4 Agarwal, R.; Barrelet, C. J.; Lieber, C. M. *Nano Lett.* **2005**, *5*, 917-920.
- 5 Saxena, D.; Mokkaapati, S.; Parkinson, P.; Jiang, N.; Gao, Q.; Tan, H. H.; Jagadish, C. *Nat. Photon.* **2013**, *7*, 963-968
- 6 Tatebayashi, J.; Kako, S.; Ho, J.; Ota, Y.; Iwamoto, S.; Arakawa, Y. *Nat. Photon.* **2015**, *9*, 501-505.
- 7 Chen, R.; Tran, T.-T. D.; Ng, K. W.; Ko, W. S.; Chuang, L. C.; Sedgwick, F. G.; Chang-Hasnain, C. *Nat. Photon.* **2011**, *5*, 170-175.
- 8 Bhattacharya, I.; Lu, F.; Malheiros-Silveira, G. N.; Deshpande, S.; Ng, K. W.; Chang-Hasnain, C. In *Room-temperature InGaAs/InP quantum-well-in-nanopillar laser directly grown on silicon*. CLEO 2016, **2016**, p SF2L.5
- 9 Mayer, B.; Janker, L.; Loitsch, B.; Treu, J.; Kostenbader, T.; Lichtmannecker, S.; Reichert, T.; Morkötter, S.; Kaniber, M.; Abstreiter, G. *Nano Lett.* **2015**, *16*, 152-156.
- 10 Li, K.; Liu, X.; Wang, Q.; Zhao, S.; Mi, Z. *Nat. Nanotechnol.* **2015**, *10*, 140-144.
- 11 Treu, J.; Speckbacher, M.; Saller, K.; Morkötter, S.; Döblinger, M.; Xu, X.; Riedl, H.; Abstreiter, G.; Finley, J.; Koblmüller, G. *Appl. Phys. Lett.* **2016**, *108*, 053110.
- 12 Mayer, B.; Rudolph, D.; Schnell, J.; Morkötter, S.; Winnerl, J.; Treu, J.; Müller, K.; Bracher, G.; Abstreiter, G.; Koblmüller, G. *Nat. Commun.* **2013**, *4*, 2931.
- 13 Ma, Y.; Guo, X.; Wu, X.; Dai, L.; Tong, L. *Adv. Opt. Photonics* **2013**, *5*, 216-273.
- 14 Yokoo, A.; Takiguchi, M.; Birowosuto, M. D.; Tateno, K.; Zhang, G.; Kuramochi, E.; Shinya, A.; Taniyama, H.; Notomi, M. *ACS Photonics* **2017**, *4*, 355-362.
- 15 Chin, A.; Vaddiraju, S.; Maslov, A.; Ning, C.; Sunkara, M.; Meyyappan, M. *Appl. Phys. Lett.* **2006**, *88*, 163115.
- 16 Kim, H.; Lee, W.-J.; Farrell, A. C.; Morales, J. S. D.; Senanayake, P.; Prikhodko, S. V.; Ochalski, T. J.; Huffaker, D. L. *Nano Lett.* **2017**, *17*, 3465-3470.
- 17 Tatebayashi, J.; Kako, S.; Ho, J.; Ota, Y.; Iwamoto, S.; Arakawa, Y. *J. Cryst. Growth* **2017**, *468*, 144-148.
- 18 Fegadolli, W. S.; Kim, S.-H.; Postigo, P. A.; Scherer, A. *Opt. Lett.* **2013**, *38*, 4656-4658.
- 19 Notomi, M.; Kuramochi, E.; Taniyama, H. *Opt. Express* **2008**, *16*, 11095.
- 20 Xu, D.-X.; Schmid, J. H.; Reed, G. T.; Mashanovich, G. Z.; Thomson, D. J.; Nedeljkovic, M.; Chen, X.; Van Thourhout, D.; Keyvaninia, S.; Selvaraja, S. K. *IEEE J. Sel. Top. Quantum Electron.* **2014**, *20*, 189-205.

- 21 Joannopoulos, J. D., Johnson, S. G., Winn, J. N. & Meade, R. D. *Photonic crystals: molding the flow of light*. Princeton university press: Princeton, 2011.
- 22 Koblmüller, G.; Abstreiter, G. *Phys. Status Solidi RRL* **2014**, *8*, 11-30.
- 23 Kim, H.; Farrell, A. C.; Senanayake, P.; Lee, W.-J.; Huffaker, D. L. *Nano Lett.* **2016**, *16*, 1833-1839.
- 24 Shapiro, J.; Lin, A.; Huffaker, D.; Ratsch, C. *Phys. Rev. B* **2011**, *84*, 085322.
- 25 Gfroerer, T. H.; Priestley, L. P.; Fairley, M. F.; Wanlass, M. W. *J. Appl. Phys.* **2003**, *94*, 1738.
- 26 Coldren, L. A., Corzine, S. W. & Mashanovitch, M. L. *Diode lasers and photonic integrated circuits*. John Wiley & Sons: New York, 2012.
- 27 Bennett, B. R.; Soref, R. A.; Del Alamo, J. A. *IEEE J. Quantum Electron.* **1990**, *26*, 113-122.
- 28 Wang, Z.; Tian, B.; Pantouvaki, M.; Guo, W.; Absil, P.; Van Campenhout, J.; Merckling, C.; Van Thourhout, D. *Nat. Photon.* **2015**, *9*, 837-842.

## Figures and Figure legends

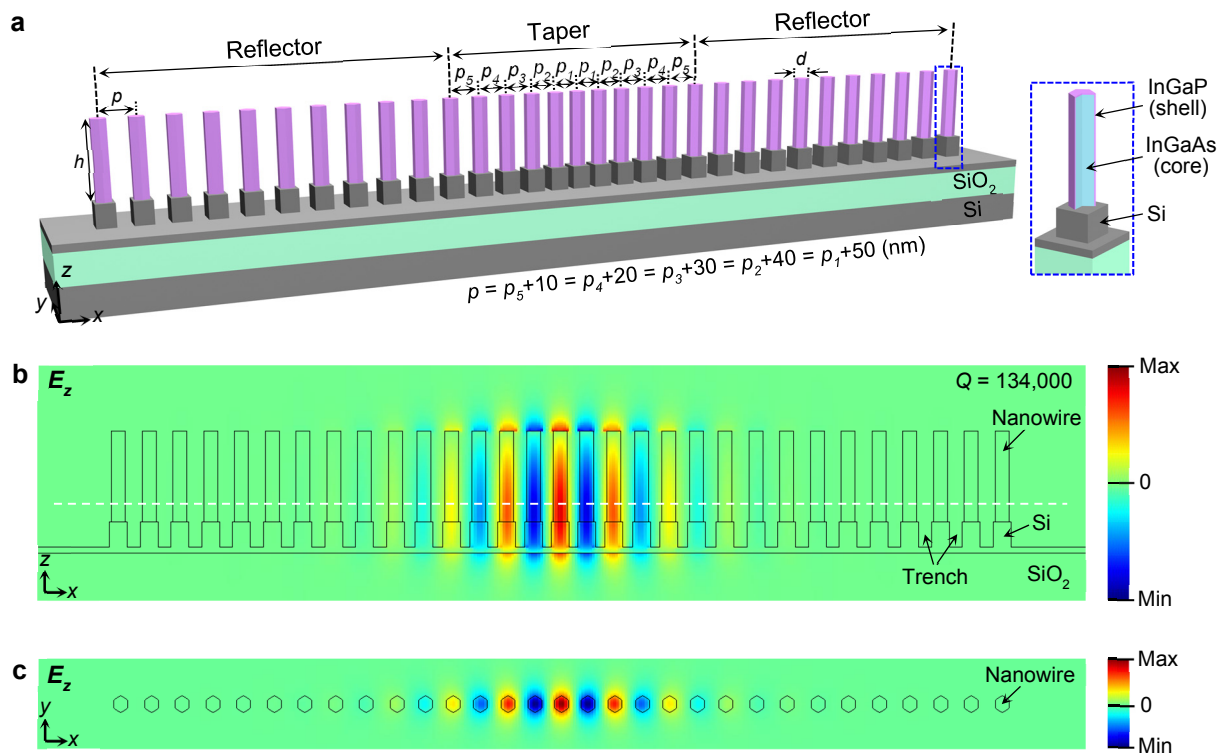


**Figure 1 | Design of bottom-up nanobeam lasers on an SOI platform.** (a) Schematic illustration of an InGaAs/InGaP core/shell nanowire array on an SOI platform. (b) Electric field profiles ( $E_z$ ) of a fundamental TM-mode in  $xz$ -plane, and (c) a horizontal cross-section along the white dashed line in **b**, both showing that the field is tightly confined in nanowires. A cavity  $Q$  of 134,000 and a resonance wavelength of 1,310 nm are obtained when  $p = 350$  nm,  $d = 180$  nm, and  $h = 700$  nm.

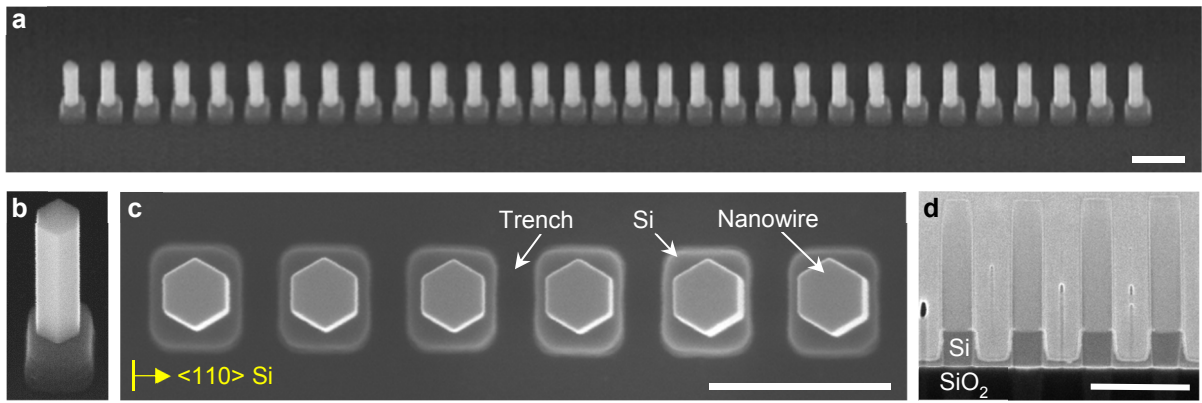


**Figure 2 | Nanowire arrays grown on an SOI platform.** (a) 35° tilted SEM images of a nanowire array cavity, and (b) a close-up view, showing high uniformity and smooth sidewalls. (c) Top-view SEM image showing the nanowires aligned to the <110> direction of the silicon layer. (d) Cross-sectional SEM image of nanowires on a patterned SOI substrate measured by slicing the sample by focused ion beam etching. Scale bars, 500 nm

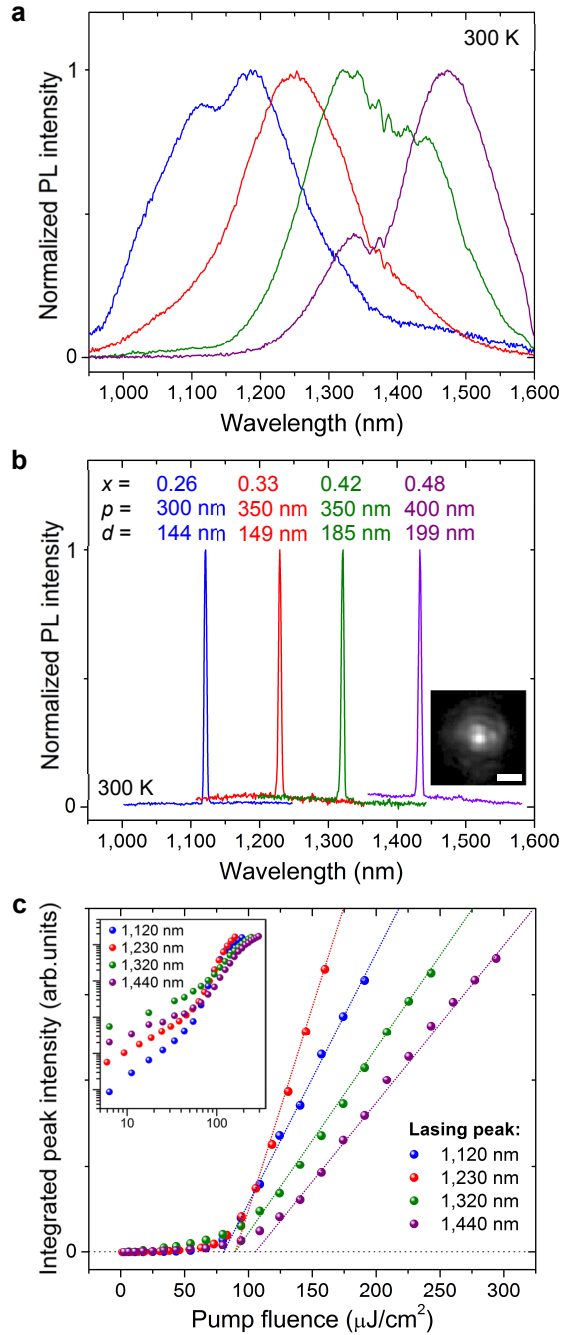


**Figure 3 | Optical characteristics of nanowire arrays at room temperature.** (a) PL spectra of InGaAs nanowires grown under different conditions.  $x$  of 0.26, 0.33, 0.42, and 0.48 are deduced from PL spectra. Atmospheric absorption around 1,150 nm and 1,400 nm distorts the shape of the PL spectra (Supporting Information Figure S9). (b) Lasing spectra of nanowire array cavities on each sample. Inset: emission pattern above lasing threshold showing an interference fringe pattern. Scale bar, 5  $\mu\text{m}$ . (c) L-L curves of nanobeam lasers in b. Lasing thresholds are estimated to be around 80–110  $\mu\text{J}/\text{cm}^2$  from the linear fitting. Inset: L-L curves plotted in a double-logarithmic scale.

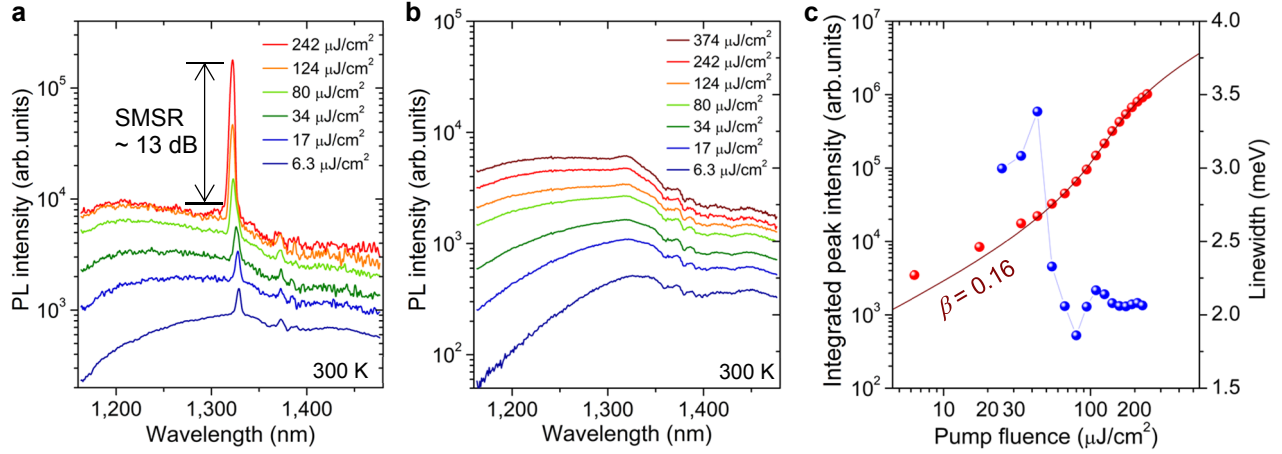


**Figure 4 | Lasing characteristics of a nanobeam laser operating at 1,320 nm.** (a) Pump power-dependent PL spectra of the  $\text{In}_{0.42}\text{Ga}_{0.58}\text{As}$  nanowire array laser, plotted in a log-scale. Spontaneous emission is clamped above the threshold, and SMSR of 13 dB is achieved at the pump fluence of  $242 \mu\text{J}/\text{cm}^2$ . (b) PL spectra of a nanowire array that does not form a cavity, showing that the spontaneous emission is not clamped by increasing the pump power. (c) Double-logarithmic L-L curve of the nanowire array laser showing an S-shape response and a sudden decrease of linewidth around lasing threshold.  $\beta$  of 0.16 is extracted from the rate equation fitting.

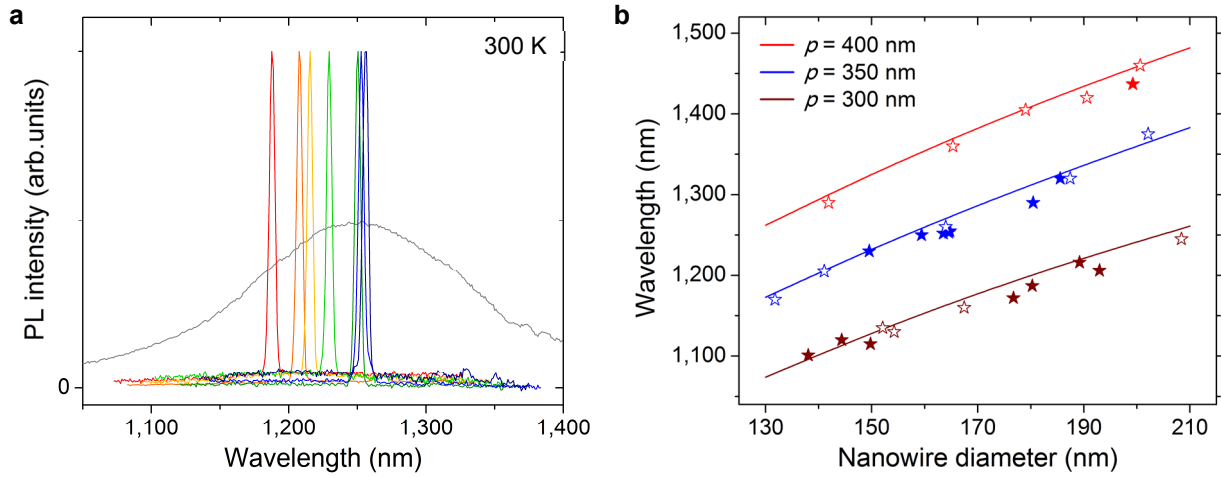


**Figure 5 | Nanobeam laser arrays with lithographically controllable operation wavelengths.** (a) Lasing spectra of seven  $\text{In}_{0.33}\text{Ga}_{0.67}\text{As}$  nanobeam laser arrays grown on two samples. A spontaneous emission spectrum (grey line) is also shown for a reference. (b) Measured lasing wavelengths of nanobeam lasers (filled stars) plotted together with FDTD simulation results (lines). Nanobeam cavities which have not reached lasing (open stars) are also shown for comparison.

Insert Table of Contents Graphic and Synopsis Here

